

EPIGENETICS

Single-molecule decoding of combinatorially modified nucleosomes

Efrat Shema,^{1,2} Daniel Jones,³ Noam Shores,² Laura Donohue,^{1,2}
Oren Ram,^{1,2} Bradley E. Bernstein^{1,2*}

Different combinations of histone modifications have been proposed to signal distinct gene regulatory functions, but this area is poorly addressed by existing technologies. We applied high-throughput single-molecule imaging to decode combinatorial modifications on millions of individual nucleosomes from pluripotent stem cells and lineage-committed cells. We identified definitively bivalent nucleosomes with concomitant repressive and activating marks, as well as other combinatorial modification states whose prevalence varies with developmental potency. We showed that genetic and chemical perturbations of chromatin enzymes preferentially affect nucleosomes harboring specific modification states. Last, we combined this proteomic platform with single-molecule DNA sequencing technology to simultaneously determine the modification states and genomic positions of individual nucleosomes. This single-molecule technology has the potential to address fundamental questions in chromatin biology and epigenetic regulation.

The activity of genes and regulatory elements is modulated by their cell type-specific chromatin organization. The fundamental building block of chromatin is the nucleosome. Nucleosomal histones are chemically modified at many amino acid positions (1, 2), which has led to the hypothesis that combinatorial marks specify distinct regulatory outcomes (the “histone code”) (3). However, our understanding of the histone code and other models (4) has been constrained by our limited ability to detect, quantify, and map combinatorially modified nucleosomes. Chromatin immunoprecipitation (ChIP), a prevalent method in chromatin biology, can identify the genomic location of a specific modification but cannot effectively distinguish whether coincident marks coexist on the same nucleosome or originate from different alleles or cells. Mass spectrometry can only compare marks if they are adjacent on the same histone peptide and does not address genomic location (5). Although alternative approaches (6), such as passing nucleosomes through nanochannels (7), show promise, they have limited throughput and/or do not provide genomic information.

We addressed these limitations by establishing a single molecule-based assay for investigating combinatorial histone modifications (Fig. 1A and figs. S1, S2, and S3). We began by isolating mononucleosomes from cells and ligating fluorescent biotinylated oligonucleotide adaptors to their free DNA ends. We captured the ligated nucleosomes in a spatially distributed manner on slides coated with polyethylene glycol (PEG) and streptavidin and incubated them with fluorescently labeled antibodies to histone modifications. We then used total internal reflection

(TIRF) microscopy to record the position and modification state of each nucleosome. As proof of principle, we captured adaptor-ligated mononucleosomes from human embryonic kidney (HEK) 293 cells and incubated them with antibody to histone H3 lysine 9 acetylation (H3K9ac). We used a TIRF microscope to simultaneously detect nucleosomes by their fluorescent adaptors (Alexa555, green) and to distinguish the subset with H3K9ac by the antibody label (Alexa647, red) (Fig. 1B).

We imaged millions of nucleosomes and decoded their modification state. We found that although the nucleosome positions were fixed, the H3K9ac antibodies repeatedly bound and dissociated at a specific subset of these nucleosome positions in a dynamic pattern (fig. S2). Summation of individual binding events over time revealed that ~1% of the nucleosomes were marked by H3K9ac (Fig. 1C). In contrast, when we treated cells with histone deacetylase (HDAC) inhibitors, the fraction of acetylated nucleosomes increased to 7% (Fig. 1, C and D). When we repeated the analysis with recombinant unmodified nucleosomes, just 0.1% of nucleosomes scored (Fig. 1E and fig. S4). We also fluorescently labeled antibodies to histone H3 lysine 4 trimethylation (H3K4me3), lysine 27 trimethylation (H3K27me3), lysine 27 dimethylation (H3K27me2), and lysine 27 acetylation (H3K27ac); we confirmed their specificities by imaging unmodified recombinant nucleosomes and marked peptides and by probing arrays of modified peptides (Fig. 1, E and F, and figs. S4 and S5).

In embryonic stem cells (ESCs), developmental gene promoters appear to be concomitantly marked by repressive (H3K27me3) and activating (H3K4me3) histone modifications (8, 9). This bivalent chromatin state has been suggested to poise these genes for alternate fates, but this remains controversial (10). Sequential ChIP and IP mass spectrometry have provided evidence for

the coexistence of the opposing marks (8, 11) but cannot definitely identify an individual bivalent nucleosome. We leveraged our single-molecule platform to quantify directly the coexistence of these key marks on nucleosomes derived from pluripotent ESCs, from ESCs differentiated to embryoid bodies (EBs), and from fully committed lung fibroblasts.

We captured nucleosomes and determined their positions as described above, chemically cleaved their fluorophores, and incubated them simultaneously with H3K4me3 (green) and H3K27me3 (red) antibodies (figs. S6 and S7). TIRF imaging revealed that ~6.5% of nucleosomes from ESCs carried H3K27me3 (Fig. 2A and figs. S8 and S9). This fraction was somewhat higher in EBs and lung fibroblasts, consistent with previous findings that this repressive mark expands during differentiation (2). The fraction of nucleosomes marked by H3K4me3 was relatively constant (ESCs, ~2%; EBs, ~1.6%; and lung, ~1.6%). Single-molecule counting revealed that 0.5% of nucleosomes in ESCs carried both marks and thus were truly bivalent (Fig. 2, A and D, and fig. S8). In contrast, in both EBs and fibroblasts, bivalent nucleosomes were much less prevalent and were depleted relative to random expectation (Fig. 2A).

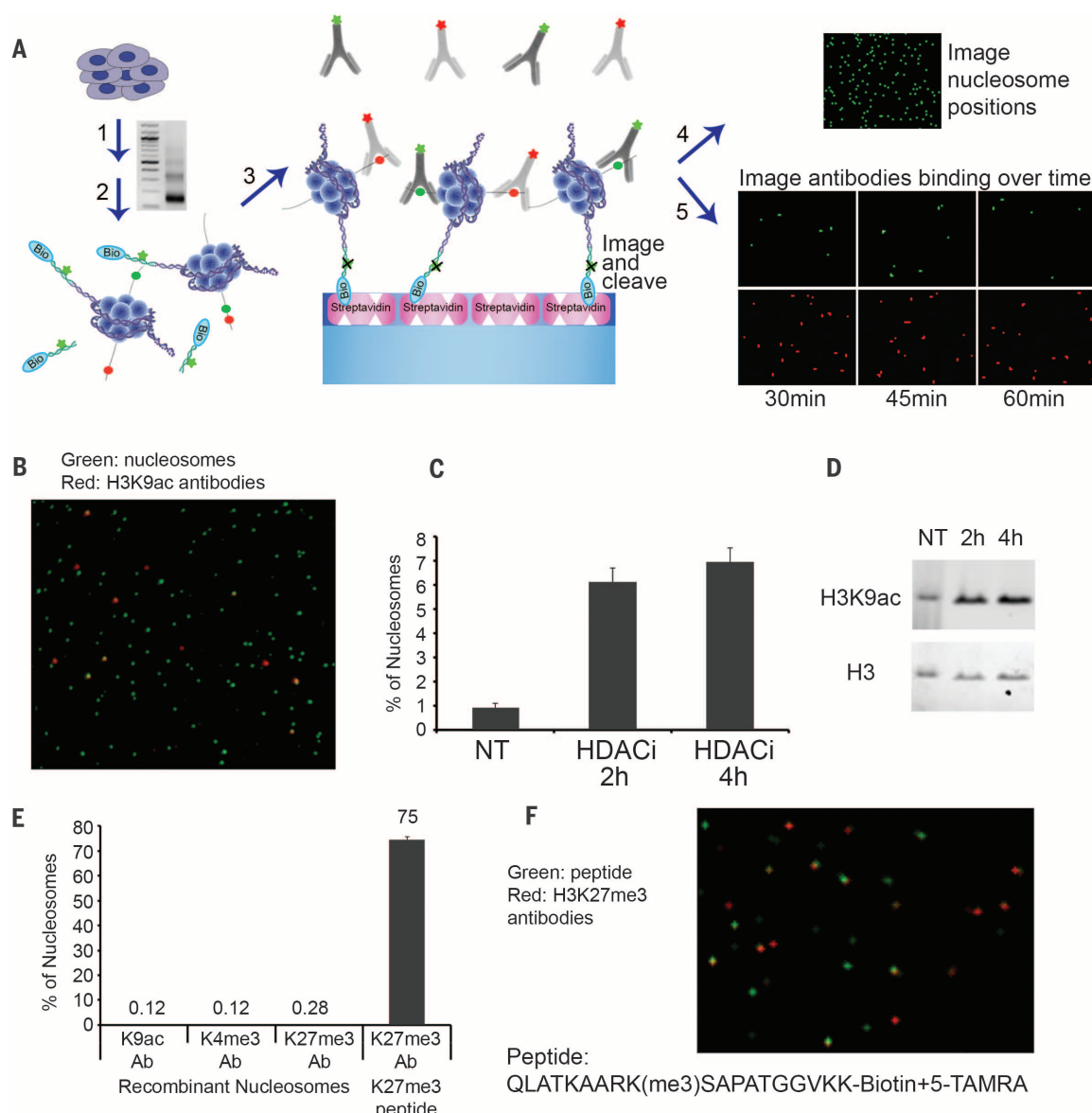
Bivalent nucleosome could reflect either the symmetric co-occurrence of H3K4me3 and H3K27me3 on the same histone tail or asymmetric marking on opposite tails. To address this, we extracted individual histone molecules from ESCs, biotinylated them, spatially distributed them on our surface, and detected H3K4me3- and H3K27me3-modified tails (Fig. 2E). We found that 0.4% of H3K27me3-modified tails also carried H3K4me3. In comparison, just 0.04% of H3K27me3-modified tails scored for H3K27ac, a combination that is chemically prohibited (fig. S8). The 10-fold excess in the detection of bivalent H3 tails relative to the background suggests that symmetric bivalent nucleosomes do exist in ESCs. Nonetheless, we estimate that 94% of bivalent nucleosomes are asymmetric, whereas just 6% are modified on the same tail (fig. S8).

Genomic loci marked by bivalent chromatin in ESCs are frequently deregulated in cancer cells (12). Moreover, the Polycomb and trithorax complexes that catalyze H3K27me3 and H3K4me3 are often mutated in cancer (12). We therefore investigated these modifications in cancer cells (Fig. 2, B and C, and fig. S8). We detected bivalent nucleosomes in three cell lines that lack known Polycomb or trithorax mutations—T cell acute leukemia (DND-41), embryonic kidney (HEK293), and glioblastoma (GSC8)—at levels higher than in our differentiated models (EB and lung) but lower than in ESCs. When we examined a leukemia line (SKM-1) with a loss-of-function (LOF) mutation of the PRC2 subunit EZH2 (13), we observed very few H3K27me3-marked nucleosomes (~1%; Fig. 2C). We also examined a lymphoma cell line (Karpas422) with a gain-of-function (GOF) EZH2 mutation that increases its catalytic activity (14); we detected H3K27me3 on ~15% of nucleosomes. Bivalent nucleosomes were prevalent in the lymphoma cells, with roughly half

¹Department of Pathology and Center for Cancer Research, Massachusetts General Hospital and Harvard Medical School, Boston, MA 02114, USA. ²Broad Institute of MIT and Harvard, Cambridge, MA 02142, USA. ³Seqlab, Woburn, MA 01801, USA.
*Corresponding author. Email: bernstein.bradley@mgh.harvard.edu

Fig. 1. Single-molecule detection of post-translational modifications on nucleosomes.

(A) Experimental approach. Step 1: Nucleosomes from cells are prepared by micrococcal nuclease digestion. The gel shows nucleosomal DNA fragments of expected lengths. Step 2: Free DNA ends are ligated to fluorescent biotinylated oligonucleotide adaptors (Bio, biotin). Step 3: Adaptor-ligated mononucleosomes are purified on a glycerol gradient and captured on PEG-streptavidin-coated slides. Step 4: Nucleosome positions on the surface are imaged by TIRF microscopy, and the fluorophore is then cleaved from the adaptor. Step 5: Attached nucleosomes are incubated with fluorescently labeled antibodies to histone modifications. Time-lapse images detect repeated binding and dissociation events and are integrated to score modified nucleosomes. Throughout the diagram, red and green circles represent histone modifications, and the corresponding stars represent fluorophores conjugated to antibodies or oligonucleotide adaptors. In (B) to (D), HEK293 cells were treated with HDAC inhibitor (HDACi) (NT, nontreated; h, hours). (B) Single-molecule detection of labeled nucleosomes (Alexa555, green) bound by labeled H3K9ac antibodies (Alexa647, red). (C) The percentage of nucleosomes marked by H3K9ac under each condition was determined by single-molecule counting (error bars, SD). (D) Western blot confirms increased H3K9ac in treated cells. In (E)



and (F), recombinant unmodified nucleosomes and H3K27me3-modified peptide were probed with the indicated antibodies (Ab). (E) The percentage of bound nucleosomes or peptides detected. (F) Single-molecule detection of labeled H3K27me3 peptide [TAMRA (5-carboxytetramethylrhodamine) green] with labeled H3K27me3 antibodies (Alexa647, red) at a single time point. Single-letter abbreviations for the amino acid residues are as follows: A, Ala; G, Gly; K, Lys; L, Leu; P, Pro; Q, Gln; R, Arg; S, Ser; T, Thr; and V, Val.

of all H3K4me3-marked nucleosomes carrying H3K27me3 (Fig. 2, C and F, and fig. S8). The proportion of bivalent nucleosomes is about four-fold greater than expected from random overlap, suggesting that the mutant EZH2 preferentially catalyzes H3K27me3 on nucleosomes that are marked by H3K4me3. This is consistent with the increased H3K27me3 over active promoters that has been observed in EZH2 GOF lymphomas (15). When we treated these lymphoma cells with an EZH2 inhibitor (16), H3K27me3 was preferentially lost from bivalent nucleosomes (Fig. 2G).

This may reflect increased nucleosome turnover and/or preferential demethylation in such regions.

We next explored higher-order combinations of H3K27ac [which marks active enhancers (2)], H3K27me2 [which marks intergenic regions (17)], H3K4me3, and H3K27me3 (Fig. 3A and fig. S11). Monitoring of four or more histone modifications on single nucleosomes was carried out in successive steps of antibody incubation and imaging, which were separated by a wash step to remove antibodies. Single-molecule counting revealed that the proportions of nucleosomes marked

by each of the four modifications were similar between ESCs and lung fibroblasts, with the exception that H3K27 methylations were modestly higher in the differentiated cells (Fig. 3A). When we considered these modifications in combination, however, we observed considerable differences between cell types (Fig. 3B and fig. S11).

ESC chromatin was enriched for the bivalent combination and for the pairwise combination of the two active marks, H3K4me3 and H3K27ac. The other pairwise combinations were present in roughly the same proportions as would be

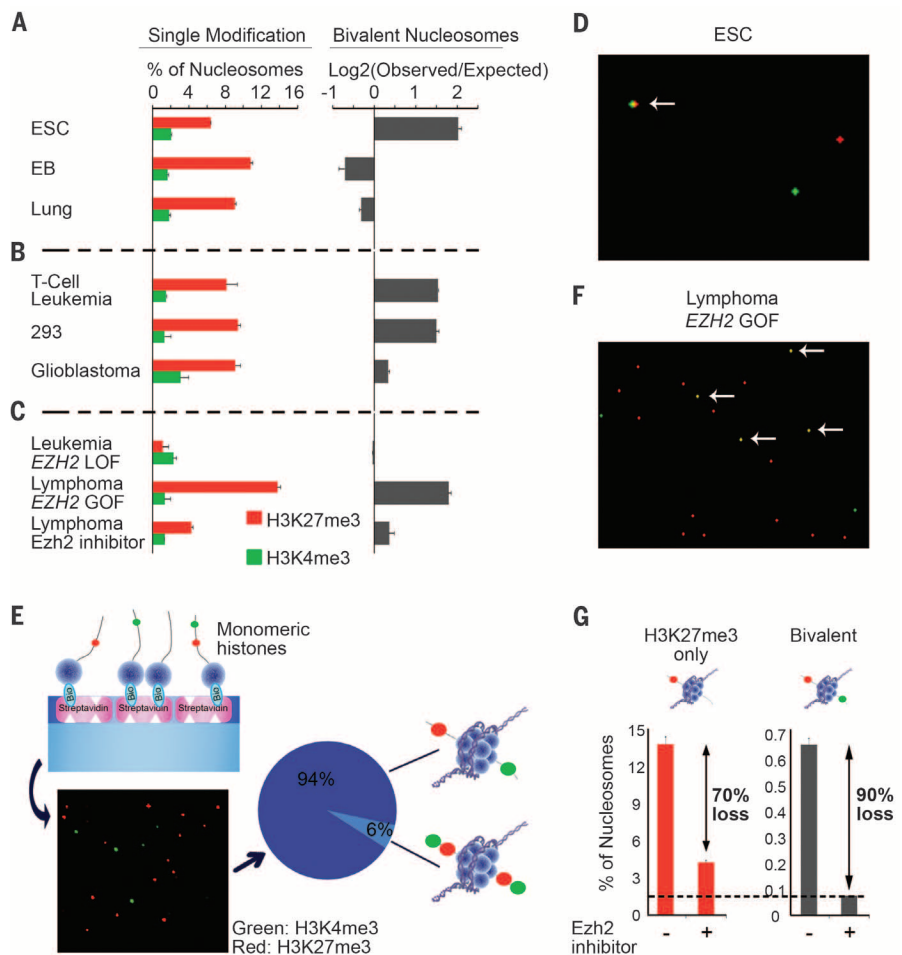


Fig. 2. Single-molecule imaging of symmetric and asymmetric bivalent nucleosomes. (A) We investigated modifications on nucleosomes from pluripotent ESCs, EBs, and lung fibroblasts. On the left, colored bars indicate percentages of nucleosomes with H3K27me3 (red) or H3K4me3 (green) (error bars, SD). On the right, black bars indicate relative over- or underrepresentation of bivalent nucleosomes. Results on the right are presented as the log₂ ratio of the observed proportion of bivalent nucleosomes to the proportion of nucleosomes with these two marks that would be expected from random association (the latter is calculated as the fraction with H3K27me3 multiplied by the fraction with H3K4me3; fig. S10). (B) Nucleosomes from a T-cell acute lymphoblastic leukemia line, from HEK293 cells, and from glioblastoma stem cells were decoded as in (A). (C) Nucleosomes from an acute leukemia line with an EZH2 LOF mutation, a lymphoma line with an EZH2 GOF mutation, and the lymphoma cells treated with EZH2 inhibitor GSK126. (D) A magnified TIRF image overlay reveals three nucleosomes, one with H3K27me3 (red), one with H3K4me3 (green), and one with concomitant bivalent modifications (arrow). (E) The diagram and image show H3K27me3 and H3K4me3 antibodies binding to individual histones isolated from ESCs. 94% of bivalent nucleosomes are asymmetric, whereas just 6% are modified on the same tail. In (F) and (G), the lymphoma cell line with the EZH2 GOF mutation was treated with GSK126 for 3 days. (F) Nucleosomes were decoded for H3K27me3 and H3K4me3. The image shown is of pretreated samples, with arrows highlighting bivalent nucleosomes. (G) Plot showing the percentages of H3K4me3-negative (H3K27me3 only; left) and H3K4me3-positive (bivalent; right) nucleosomes carrying H3K27me3 (error bars, SD). Bivalent nucleosomes were more likely to lose H3K27me3 after treatment with GSK126.

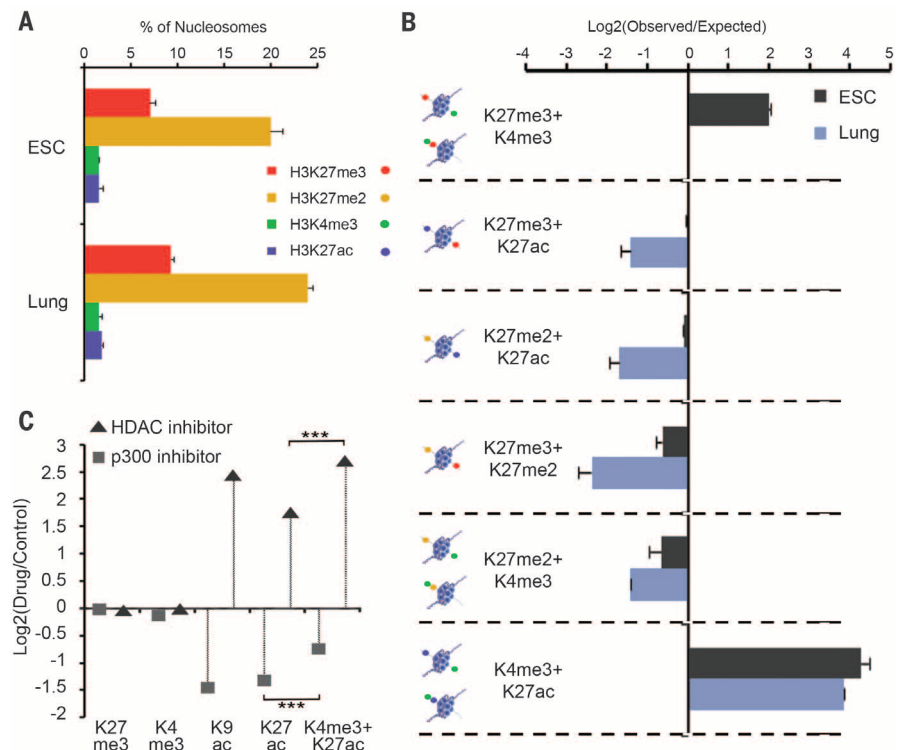


Fig. 3. Higher-order modification states across cellular states and inhibitor treatments. (A) Individual nucleosomes from ESCs and lung fibroblasts were decoded for H3K4me3, H3K27me3, H3K27me2, and H3K27ac, as described in Fig. 1. Bars depict the percentage of nucleosomes with the indicated modification (error bars, SD). (B) Bars indicate the relative over- or underrepresentation of each possible modification pair, relative to random expectation, as in Fig. 2A. Opposing modifications were relatively more likely to coexist in ESCs than in lung fibroblasts. (C) ESCs were treated with dimethyl sulfoxide (control), HDAC inhibitor (sodium butyrate), or p300 inhibitor (C646). Nucleosomes were isolated and decoded for H3K27me3, H3K4me3, H3K9ac, and H3K27ac. The plot shows the effects of the inhibitors on each single modification and on the combination of H3K27ac and H3K4me3. ***P < 0.001.

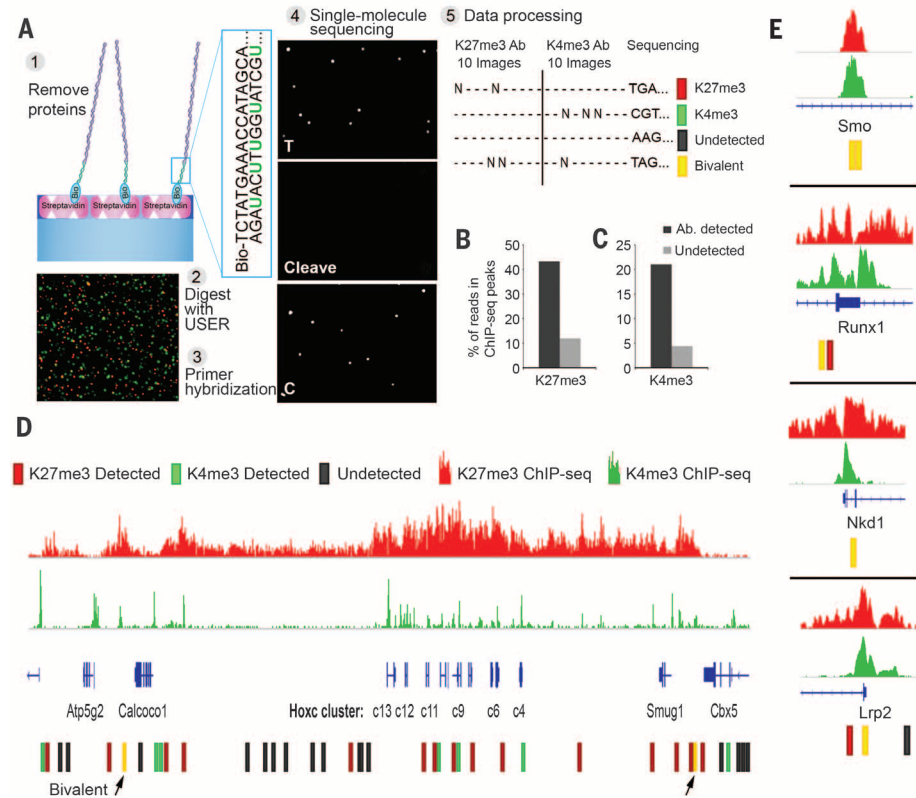


Fig. 4. Single-molecule sequencing determines genomic positions of modified nucleosomes.

(A) Experimental approach. Step 1: Nucleosomes are captured and probed for their modification state, as in Fig. 1A. Histones are evicted by increasing salt concentration. Step 2: The enzyme USER (uracil-specific excision reagent) is applied to excise uracil bases incorporated into the nonbiotinylated adaptor strand and expose a known sequence. Step 3: Complementary primer is hybridized to the adaptor. The image shows single-molecule detection of nucleosomal DNA (Alexa647, red) and primer (Alexa555, green). Step 4: Direct single-molecule DNA sequencing-by-synthesis is performed (22). The images reflect two sequencing cycles, covering the incorporation of thymine, the cleavage of the fluorophore and terminator, and the incorporation of cytosine. Step 5: For each *x,y* coordinate on the surface, sequence data are analyzed and integrated with the initial images that scored the antibody binding and modification states of the corresponding nucleosomes. (B) Single-molecule reads were aligned to the genome. The plot shows percentages of H3K27me3-modified nucleosome reads (detected) or unmodified nucleosome reads (undetected) that aligned to H3K27me3-enriched regions per conventional ChIP-seq. (C) Percentages of H3K4me3-modified nucleosome reads that aligned to H3K4me3-enriched regions per conventional ChIP-seq. (D) Gene annotations (blue) for the HOXC gene cluster are shown with H3K27me3 and H3K4me3 ChIP-seq tracks. Single-molecule reads that aligned to these regions are indicated, along with the modification status of the corresponding nucleosome. (E) Analogous data for other developmental loci for which bivalent nucleosomes were definitely identified.

expected from chance overlap. The lung fibroblasts were enriched for the pairwise combination of active marks, like the ESCs, but not for the bivalent nucleosomes. However, the lung fibroblast chromatin was depleted for the other combinations (Fig. 3B), including the three pairwise states for H3K27 modifications, which are by definition asymmetric. These distinct combinatorial modification patterns probably relate to different chromatin environments in the respective cell types, particularly the hyperdynamic nature of ESC chromatin (fig. S12) (18).

We next examined how combinatorial chromatin states change upon treatment with a pan-HDAC inhibitor or with a p300 histone acetyltransferase inhibitor. HDAC inhibition signifi-

cantly increased levels of H3K9ac and H3K27ac, whereas p300 inhibition had the opposite effect (Fig. 3D and fig. S11). Neither treatment altered H3K4me3 or H3K27me3. However, the changes in histone acetylation occurred preferentially on nucleosomes with specific markings. In the case of HDAC inhibition, increased acetylation preferentially affected H3K4me3-marked nucleosomes, consistent with the modulation of acetylation levels by HDACs at active promoters (19). In contrast, H3K4me3-marked nucleosomes were less affected by p300 inhibition, consistent with a role for this enzyme at enhancers (20).

Phosphorylation of the histone variant H2AX (γ H2AX) is one of the earliest and best-studied marks of DNA damage. We therefore examined

γ H2AX levels on individual nucleosomes extracted from ESCs. We found that ~2% of the nucleosomes contained γ H2AX at baseline (fig. S13). Combinatorial analysis revealed that γ H2AX was specifically enriched on nucleosomes with activating marks (H3K27ac and H3K4me3). Treatment with HDAC inhibitors led to concomitant increases in acetylation and γ H2AX levels, consistent with studies documenting high baseline levels of γ H2AX associated with decondensed chromatin in ESCs (21).

Last, we used single-molecule sequencing technology to read the DNA associated with each individual nucleosome (Fig. 4A and fig. S14). We captured adaptor-ligated nucleosomes from ESCs and queried their H3K27me3 and H3K4me3 status. We then displaced the histone octamers, leaving behind double-stranded nucleosomal DNA. We enzymatically cleaved the uracil bases that were incorporated into the nonbiotinylated strand of the adaptor, exposing a known sequence that was used as a priming site for single-molecule sequencing-by-synthesis (22). We used TIRF microscopy to detect repeated cycles of base addition, separated by chemical cleavage of the fluorescent label and terminator.

Integration of TIRF images for antibody-based detection of modifications with subsequent sequencing reaction data collected on the same flow cell allowed us to coordinately determine the modification state and DNA sequence of each nucleosome (Fig. 4). More than 80% of the ~300,000 reads aligned to the mouse genome. We then compared the genomic localization of individual nucleosomes with their modification states. Of the ~26,000 reads for which the corresponding nucleosomes scored positively for H3K27me3, 45% aligned to genomic regions within H3K27me3 ChIP sequencing (ChIP-seq) peaks (Fig. 4B). This is consistent with the 30 to 50% of reads that map to enriched intervals in a typical H3K27me3 ChIP-seq experiment. In comparison, just 12% of H3K27me3-negative nucleosomes aligned to H3K27me3 ChIP-seq peaks. In a subset of these experiments, we probed the sequenced nucleosomes for both H3K27me3 and H3K4me3, yielding ~1000 aligned reads for concomitantly marked molecules and thus providing the first definitive localization of individual bivalent nucleosomes (Fig. 4, D and E).

We have taken a critical step toward defining the nature and importance of combinatorial chromatin modifications. We used single-molecule technology to decode concurrent modifications on individual nucleosomes and sequence the associated DNA. We identified individual bivalent nucleosomes with concomitant repressive and activating marks and mapped their genomic locations. We also documented other combinatorial modification states whose proportions change during cellular specification or upon treatment with epigenetic inhibitors. The single-molecule assay that we describe here requires little starting material and is highly scalable, given that many millions or even billions of nucleosomes may be decoded and sequenced in an automated imaging run.

REFERENCES AND NOTES

1. C. M. Rivera, B. Ren, *Cell* **155**, 39–55 (2013).
2. A. J. Bannister, T. Kouzarides, *Cell Res.* **21**, 381–395 (2011).
3. T. Jenuwein, C. D. Allis, *Science* **293**, 1074–1080 (2001).
4. J. S. Lee, E. Smith, A. Shilatifard, *Cell* **142**, 682–685 (2010).
5. S. Sidoli, B. A. Garcia, *Proteomics* **15**, 2901–2902 (2015).
6. D. Gomez, L. S. Shankman, A. T. Nguyen, G. K. Owens, *Nat. Methods* **10**, 171–177 (2013).
7. P. J. Murphy et al., *Proc. Natl. Acad. Sci. U.S.A.* **110**, 7772–7777 (2013).
8. B. E. Bernstein et al., *Cell* **125**, 315–326 (2006).
9. V. Azuara et al., *Nat. Cell Biol.* **8**, 532–538 (2006).
10. P. Voigt, W. W. Tee, D. Reinberg, *Genes Dev.* **27**, 1318–1338 (2013).
11. P. Voigt et al., *Cell* **151**, 181–193 (2012).
12. S. B. Baylin, P. A. Jones, *Nat. Rev. Cancer* **11**, 726–734 (2011).
13. T. Ernst et al., *Nat. Genet.* **42**, 722–726 (2010).
14. D. B. Yap et al., *Blood* **117**, 2451–2459 (2011).
15. W. Béguin et al., *Cancer Cell* **23**, 677–692 (2013).
16. M. T. McCabe et al., *Nature* **492**, 108–112 (2012).
17. K. J. Ferrari et al., *Mol. Cell* **53**, 49–62 (2014).
18. E. Meshorer, T. Misteli, *Nat. Rev. Mol. Cell Biol.* **7**, 540–546 (2006).
19. O. Ram et al., *Cell* **147**, 1628–1639 (2011).
20. N. D. Heintzman et al., *Nat. Genet.* **39**, 311–318 (2007).
21. V. Turinotto, C. Giachino, *Nucleic Acids Res.* **43**, 2489–2498 (2015).
22. T. D. Harris et al., *Science* **320**, 106–109 (2008).

ACKNOWLEDGMENTS

We thank I. Tiros, P. Blainey, K. Xiong, and S. Elledge for constructive discussions; J. Reifenberger for help with imaging technology; M. Bray for help with image analysis; I.-S. Kim, K. Bouazoune, C. Epstein, and J. Kaur for their experimental contributions; and S. Deindl, B. Liu, and R. Ryan for valuable experimental advice. E.S. is supported by the Jane Coffin Childs Memorial Fund for Medical Research. D.J. is partially supported by

National Human Genome Research Institute–Small Business Innovation Research grant R44HG005279. This research was supported by funds from the National Human Genome Research Institute, the Klarman Cell Observatory, and the Howard Hughes Medical Institute. Sequencing data are available in the supplementary materials (database S1). D.J. is a founder and the president of SeqLL, which contributed to the technologies described in this study. E.S., D.J., and B.E.B. have filed a provisional patent covering single-molecule methodologies described in the paper.

SUPPLEMENTARY MATERIALS

www.sciencemag.org/content/352/6286/717/suppl/DC1
Materials and Methods
Figs. S1 to S4
References (23–28)
Database S1
29 October 2015; accepted 6 April 2016
10.1126/science.aad7701

CELL BIOLOGY

Microtubule doublets are double-track railways for intraflagellar transport trains

Ludek Stepanek and Gaia Pigino*

The cilium is a large macromolecular machine that is vital for motility, signaling, and sensing in most eukaryotic cells. Its conserved core structure, the axoneme, contains nine microtubule doublets, each comprising a full A-microtubule and an incomplete B-microtubule. However, thus far, the function of this doublet geometry has not been understood. We developed a time-resolved correlative fluorescence and three-dimensional electron microscopy approach to investigate the dynamics of intraflagellar transport (IFT) trains, which carry ciliary building blocks along microtubules during the assembly and disassembly of the cilium. Using this method, we showed that each microtubule doublet is used as a bidirectional double-track railway: Anterograde IFT trains move along B-microtubules, and retrograde trains move along A-microtubules. Thus, the microtubule doublet geometry provides direction-specific rails to coordinate bidirectional transport of ciliary components.

The cilium is a conserved organelle that plays a fundamental role in signaling, sensing, and motility. Cilia have a complex microtubule-based structure that is not found in other cellular compartments. This structure includes nine peripheral microtubule doublets, each comprising a complete A-tubule and an incomplete B-tubule. However, the function of this distinctive conserved geometry has so far been unknown.

In addition to serving as platforms for periodically arranged axonemal proteins and protein complexes, ciliary microtubule doublets function as railways for intraflagellar transport (IFT), the process required for the assembly and disassembly of the cilium (1). Large protein complexes, known as IFT trains (2, 3), rapidly traverse up and down

the cilium to move ciliary building blocks between the cell body and the ciliary distal tip (4–7), where the assembly of the cilium takes place. Electron microscopy (EM) shows that IFT trains move along the doublets while keeping contact with the ciliary membrane (2, 3, 8). It has thus far been unclear, however, how the IFT machinery is organized to avoid collisions between anterograde and retrograde trains.

In trypanosome flagella, anterograde IFT trains move at different speeds and can approach each other and fuse, similar to trains shunting, suggesting that anterograde trains might travel on a restricted set of axonemal microtubule doublets (9). No such interactions are observed between retrograde trains, nor do trains moving in opposite directions collide. To further analyze the dynamics and potential interactions of IFT trains in cilia, we imaged green fluorescent protein (GFP)-tagged trains in *Chlamydomonas* cells by means of total internal reflection fluorescence (TIRF) microscopy (fig. S1 and movies S1, S2,

and S3). As expected, we observed anterograde–anterograde and retrograde–retrograde train interactions. Typically, a faster train caught up with a slower one moving in the same direction and both would then progress together at the same speed (fig. S1 and movies S2 and S3). Thus, it appears that IFT trains moving in the same direction often share the same microtubule rail. We never observed collisions between trains that traveled in opposite directions (supplementary text). Because oppositely directed trains passed by each other without changes in the direction of motion (fig. S1), a mechanism must exist to prevent collisions.

Although it is possible that trains could switch to another microtubule when they encounter a train moving in the opposite direction, this would be predicted to cause deceleration, which was not evident in our kymographs (see also the supplementary text). In trypanosomes, IFT trains avoid microtubule doublets that contact the paraflagellar rod (10), raising the possibility that IFT trains can recognize specific microtubule doublets. This could allow anterograde and retrograde trains to use different axonemal microtubules. However, the resolution required to test this hypothesis cannot be achieved with TIRF microscopy. Only EM offers sufficient resolution to see detailed interactions between IFT trains and microtubules. Previous EM work, comparing IFT trains from flagella of wild-type cells and from those of mutant cells with defective IFT, has suggested that anterograde and retrograde trains can be distinguished on the basis of ultrastructure and size (8). Long and short IFT trains have been proposed to be associated with anterograde and retrograde transport, respectively (8). However, the lack of dynamic information has precluded a definitive interpretation of the directionality of IFT trains.

To overcome the technical limitations of static EM, we developed a correlative light and EM (CLEM) approach. Because the currently available CLEM techniques (11) do not provide sufficient spatiotemporal resolution to analyze IFT trains, which move at 2.5 to 4 $\mu\text{m}/\text{s}$, we developed a novel method that allows millisecond resolution in correlative TIRF and three-dimensional (3D) EM

Max Planck Institute of Molecular Cell Biology and Genetics (MPI-CBG), Pfotenhauerstraße 108, 01307 Dresden, Germany.

*Corresponding author. Email: pigino@mpi-cbg.de